



LAWRENCE
LIVERMORE
NATIONAL
LABORATORY

Structure of Oxide Nanoparticles in Fe-16Cr MA/ODS Ferritic Steel

L. Hsiung, M. Fluss, A. Kimura

April 7, 2010

Materials Letters

Disclaimer

This document was prepared as an account of work sponsored by an agency of the United States government. Neither the United States government nor Lawrence Livermore National Security, LLC, nor any of their employees makes any warranty, expressed or implied, or assumes any legal liability or responsibility for the accuracy, completeness, or usefulness of any information, apparatus, product, or process disclosed, or represents that its use would not infringe privately owned rights. Reference herein to any specific commercial product, process, or service by trade name, trademark, manufacturer, or otherwise does not necessarily constitute or imply its endorsement, recommendation, or favoring by the United States government or Lawrence Livermore National Security, LLC. The views and opinions of authors expressed herein do not necessarily state or reflect those of the United States government or Lawrence Livermore National Security, LLC, and shall not be used for advertising or product endorsement purposes.

Structure of Oxide Nanoparticles in Fe-16Cr MA/ODS Ferritic Steel

Luke L. Hsiung^{1*}, Michael J. Fluss¹, and Akihiko Kimura²

¹Lawrence Livermore National Laboratory
L-352, P.O. Box 808
Livermore, CA, U.S.A.

²Institute of Advanced Energy
Kyoto University, Gokasho, Uji
Kyoto 611-0011, Japan

Keywords: Mechanical alloying; Nanostructure; Crystallization; High-Resolution Electron Microscopy

ABSTRACT

Oxide nanoparticles in Fe-16Cr ODS ferritic steel fabricated by mechanical alloying (MA) method have been examined using high-resolution transmission electron microscopy (HRTEM) techniques. A partial crystallization of oxide nanoparticles was frequently observed in as-fabricated ODS steel. The crystal structure of crystalline oxide particles is identified to be mainly $Y_4Al_2O_9$ (YAM) with a monoclinic structure. Large nanoparticles with a diameter larger than 20 nm tend to be incoherent and have a nearly spherical shape, whereas small nanoparticles with a diameter smaller than 10 nm tend to be coherent or semi-coherent and have faceted boundaries. The oxide nanoparticles become fully crystallized after prolonged annealing at 900 °C. These results lead us to propose a three-stage formation mechanism of oxide nanoparticles in MA/ODS steels.

INTRODUCTION

Development of high-performance structural materials for first wall and breeding-blanket components, which will be exposed to high fluxes of high energy (14 MeV) neutrons from the deuterium-tritium fusion, is one of the major challenges in materializing future fusion reactors. The choice of structural materials for the first wall and blanket to a large degree dictates the design of the reactor systems. The selection of suitable structural materials is based on conventional properties (such as thermophysical, mechanical, and corrosion and compatibility), low neutron-induced radioactivity, and resistance to radiation-induced damage phenomena like material hardening/embrittlement and/or dimensional instability caused by void- and helium-driven swelling [1]. Oxide dispersion strengthened (ODS) F/M and ferritic steels, which produced by mechanical alloying the elemental (or pre-alloyed) metallic powder and yttria (Y_2O_3) oxide powder consolidated by hot extrusion or hot isostatic pressing, are advanced structural materials with a potential to be used at elevated temperatures due to the dispersion of thermally stable oxide nanoparticles into the F/M matrix. The use of ODS steels should improve creep strength and oxidation/corrosion resistance at high temperatures and consequently increase the operating temperature of first wall and blanket structures in the future fusion reactors by approximately 700 °C or higher [2]. The performance of ODS steels is largely determined by the particle size and the stability of dispersed oxide nanoparticles. Although Y_2O_3 has been selected as the major dispersed oxide, its particle size increases during the consolidation and thermomechanical treatment of ODS steels. To enhance the stability of oxide particles, titanium and aluminum are added to

* Corresponding author. Tel.: +1-925 424 3125; fax: +1-925 424 3815
E-mail address: hsjung1@llnl.gov (L. Hsiung).

form complex oxide with Y_2O_3 so as to make the dispersed oxides finer and more stable [2, 3]. A complex formation mechanism involving fragmentation, dissolution of Y_2O_3 particles, and precipitation of complex-oxide nanoparticles were previously proposed by Okuda and Fujiwara [4], Kimura et al. [5] and Sakasegawa et al. [6] based on the results generated from x-ray diffraction and conventional TEM studies. However, recent studies conducted by Marquis [7] using 3-D atom probe tomography and Klimiankou et al. [8] using EDX and EELS methods revealed that oxide nanoparticles in various as-fabricated ODS steels (MA957, 12Cr-ODS, and Eurofer 9Cr-ODS) contained yttrium complex-oxide core structures in association with solute-enriched shell structures. The existence of core/shell structures in nanoparticles however challenges the accountability of dissolution/precipitation formation mechanism. HRTEM study of nanoparticles in Fe-16Cr ODS ferritic steel was therefore conducted to investigate the structure of oxide nanoparticles in order to better understand the formation mechanism of oxide nanoparticles in mechanically alloyed ODS steels.

EXPERIMENTAL

The material used for this investigation was Fe-16Cr-4Al-2W-0.3Ti-0.3 Y_2O_3 ferritic steel, which is designated as 16Cr-ODS steel hereafter. Details of the fabrication process for MA/ODS steels can be found elsewhere [9]. Briefly, the pre-alloyed powder was first mechanically alloyed with Y_2O_3 powder in an Argon gas atmosphere at room temperature using an attrition type ball mill. The powder was then sealed in a stainless-steel can and degassed at 400 °C in 0.1 Pa pressure. The canned powders were subsequently consolidated by a hot extrusion technique at 1150 °C. After the extrusion, the consolidated ODS steel was thermally treated at 1050 °C for 1 hour. One ODS steel sample was also annealed at 900 °C, 168 hours (one week) for a thermal stability study. The chemical composition (in wt.%) of the consolidated material is C: 0.08, Si: 0.033, Cr: 16, W: 1.82, Al: 4.59, Ti: 0.28, Y_2O_3 : 0.368, and Fe: balance [10]. Thin foils for TEM analysis were prepared by a standard procedure that includes slicing, grinding, and polishing the recovered fragments with the foils surface approximately perpendicular to the loading axis. Final thinning of the foils was performed using a standard twin-jet electropolishing technique in an electrolyte (90 vol.% acetic acid, 10 vol.% perchloric acid) at 30 V and room temperature. Microstructural characterization was performed using Phillips CM300 field-emission transmission electron microscope (accelerating voltage of 300 kV). A software package CaRIne Crystallography 3.1 was used to simulate electron diffraction patterns in order to identify the crystal structures of oxide nanoparticles in the 16Cr-ODS steel.

RESULTS AND DISCUSSION

Typical microstructures of 16Cr-ODS steel are shown in Figs. 1a and 1b. Here elongated grains (Fig. 1a) and dense oxide nanoparticles (Fig. 1b), mainly $Y_4Al_2O_9$ (YAM) complex oxide, were observed. The sizes of oxide nanoparticles examined using energy-filtered electron microscopy (Fig. 1c) are mostly ranging from 1.7 nm to 30 nm. A mean particle size is 5.91 nm, and a particle density is $1.33 \times 10^{22} \text{ m}^{-3}$. Here the orientation relationship between $Y_4Al_2O_9$ oxide phase and the matrix can be derived from the selected-area diffraction pattern: $(0\bar{1}1)_\alpha \parallel (2\bar{4}2)_{YAM}$ and $[011]_\alpha \parallel [432]_{YAM}$. The formation of $Y_4Al_2O_9$ oxide particles was identified and confirmed by matching several observed and simulated diffraction patterns of different zone axes, and an example is shown in Fig. 1d for the $[432]_{YAM}$ -zone pattern. $Y_4Al_2O_9$ has a monoclinic structure and space group: $P2_1/c$ with $a = 0.7375 \text{ nm}$, $b = 1.0507 \text{ nm}$, $c = 1.1113 \text{ nm}$, and $\beta = 108.58^\circ$ [11, 12]. By comparing the $Y_4Al_2O_9$ nanoparticles formed in the 16Cr-ODS steel with the starting Y_2O_3 particles (space group: Ia_3 , a cubic structure with $a_0 = 1.06 \text{ nm}$ [12], and nominal particle size: 15-30 nm [13]) used to fabricate the ODS steel, one can realize that the

formation of oxide nanoparticles in ODS steels does not take place simply through a fragmentation process. The formation of $Y_4Al_2O_9$ nanoparticles indicates the occurrence of an internal oxidation reaction: $2Y_2O_3 + Al_2O_3 \rightarrow Y_4Al_2O_9$ during the MA process, which is determined by the oxygen affinity of alloying elements. That is, the formation of Y-Al-O complex oxide is predominant when both Al and Ti are present in ODS steels [3]. HRTEM images of a large ($d > 20$ nm) and a small ($d < 10$ nm) nanoparticles in a 16Cr-ODS steel sample are shown in Figs. 2a and 2b. As can be seen in Fig. 2a, the large nanoparticle tends to be nearly spherical in shape and is incoherent with the matrix. In addition, one can also distinguish the upper region of the particle with sharp lattice fringes from the lower region of the particle with a featureless appearance, which is presumably caused by a partial crystallization of the particle. On the other hand, ledges and facets can be seen at the interface between the small nanoparticle and the matrix shown in Fig. 2b, which indicates that the small nanoparticle tends to be coherent or semi-coherent with the matrix. Figure 3a shows the nucleation of a crystalline $Y_4Al_2O_9$ domain (2×5 nm in size) within an amorphous oxide particle. Orientation relationship between the crystalline $Y_4Al_2O_9$ domain and the matrix, which is the same as that shown in Fig. 1, can be derived from the fast Fourier transformation (FFT) image: $(0\bar{1}1)_\alpha \parallel (2\bar{4}2)_{YAM}$ and $[011]_\alpha \parallel [432]_{YAM}$. Figure 3b shows the interfacial structure of the crystalline $Y_4Al_2O_9$ domain and the matrix. Facets, ledges, and thin layer of amorphous domains (marked by red arrows) are typical features that can be found at the interface.

Figure 4 shows the result of a 16Cr-ODS steel sample annealed at 900 °C for 168 hours. Here a small nanoparticle remains faceted (Fig. 4a) and a large nanoparticle becomes perfectly spherical and fully crystallized (Fig. 4b), which seems to indicate that the core/shell structures of oxide nanoparticles formed in as-fabricated ODS steels [7, 8] are far from chemical equilibrium. Since solid-state amorphization induced by MA is known as one of the non-equilibrium processing routes to produce amorphous materials [14], a revised three-stage formation mechanism of oxide nanoparticles is accordingly proposed based on the above HRTEM observations: (1) Fragmentation of starting Y_2O_3 particles to form finely-dispersed (nano or sub-nano) fragments during the early stages of ball milling; (2) Agglomeration and amorphization of fragments mixed with matrix material to form clusters and agglomerates (designated as [MYO], M: alloying elements) during the later stages of ball milling; (3) Crystallization of the amorphous oxide agglomerates to form oxide nanoparticles with a complex-oxide core and a solute-enriched (M') shell. The contents of complex-oxide core and solute-enriched shell are dependent on the compositions of different ODS steels. Y-Al complex-oxide ($Y_xAl_yO_z$) cores can form in Al-contained ODS steels such as the currently studied 16Cr-ODS and MA956 steels, Y-Ti complex-oxide ($Y_xTi_yO_z$) cores can form in Ti-contained ODS steels with no addition of Al such as MA957 steel, and Y_2O_3 cores can form in ODS steels with no additions of Al and Ti such as Eurofer 9Cr-ODS steel. The solute-enriched shells can be perceived as a result of the depletion of the solutes that are not involved in the internal oxidation reactions for the complex-oxide cores such as Cr-enriched shells in the nanoparticles of MA957 and Mn- and V-enriched shells in the nanoparticles of Eurofer 9Cr-ODS steel [7, 8]. The shell thickness is likely dependent on the size of nanoparticles since the larger the particle the more matrix constituents will participate in the agglomeration and amorphization stage and thus more solutes will be depleted from the oxide cores during the crystallization of nanoparticles.

Summary

The oxide nanoparticles formed in 16Cr-ODS steel are mainly $Y_4Al_2O_9$ (YAM) with a monoclinic structure, $a = 0.7375$ nm, $b = 1.0507$ nm, $c = 1.1113$ nm, and $\beta = 108.58^\circ$. Large nanoparticles ($d > 20$ nm) usually have a nearly spherical shape and tend to be incoherent with the matrix; small nanoparticles ($d < 10$ nm) usually accompany with facets and ledges at the oxide/matrix interfaces and tend to be coherent or semi-coherent with the matrix. A structure of $Y_4Al_2O_9$ crystalline core associated with amorphous shell was observed in both large and small nanoparticles in as-fabricated 16Cr-ODS steel. The crystalline/amorphous (core/shell) structure of nanoparticles becomes vanished after prolonged annealing at 900°C for 168 hours, which suggests that the core/shell structure of oxide nanoparticles is far from chemical equilibrium. A three-stage formation mechanism of oxide nanoparticles is accordingly proposed to rationalize the core/shell structures of nanoparticles observed in several as-fabricated ODS steels.

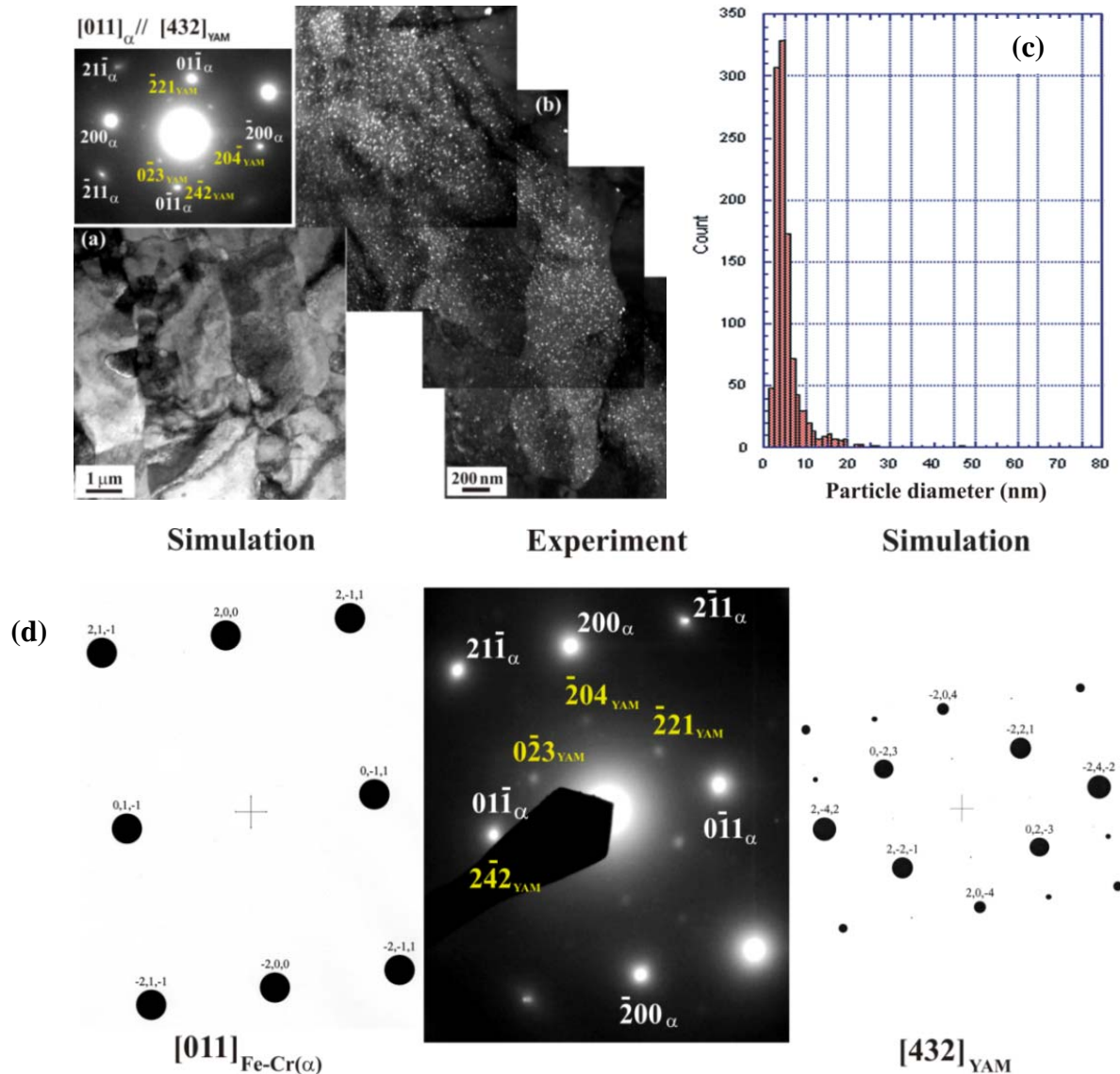


Fig. 1. (a) A bright-field TEM image shows a typical grain morphology of 16Cr-ODS steel, (b) a dark-field TEM image and a selected-area diffraction pattern of the $[011]_{Fe-Cr(\alpha)} \parallel [432]_{YAM}$ -zone show the formation of dense $Y_4Al_2O_9$ nanoparticles in 16Cr-ODS steel, (c) the size distribution of oxide nanoparticles in 16Cr-ODS steel measured using energy-filtered microscopy, (d) the observed and simulated diffraction patterns of the $[011]_{Fe-Cr(\alpha)}$ -zone and the $[432]_{YAM}$ -zone.

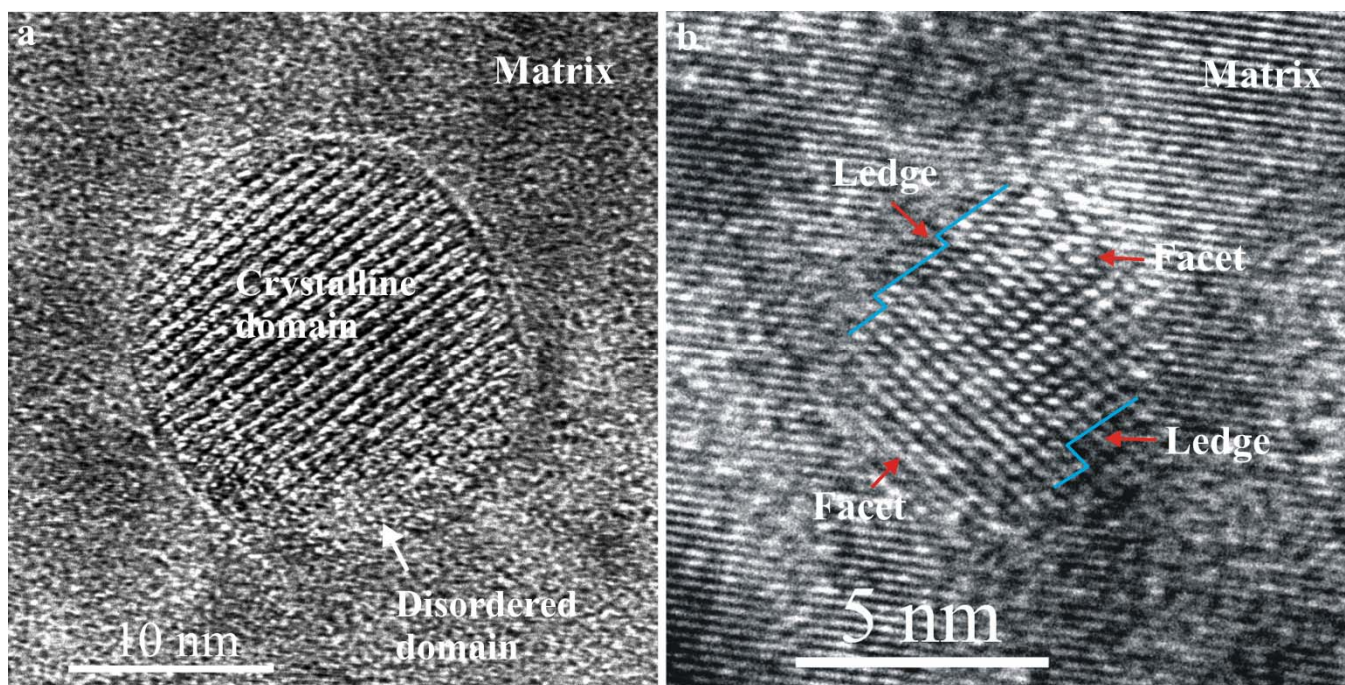


Fig. 2. HRTEM images of (a) a large nanoparticle ($d > 20$ nm): an incoherent interface associated with an eccentric core/shell (partial crystalline) structure and (b) small nanoparticles ($d < 10$ nm): a semi-coherent interface in association with facets and ledges that were outlined with blue lines.

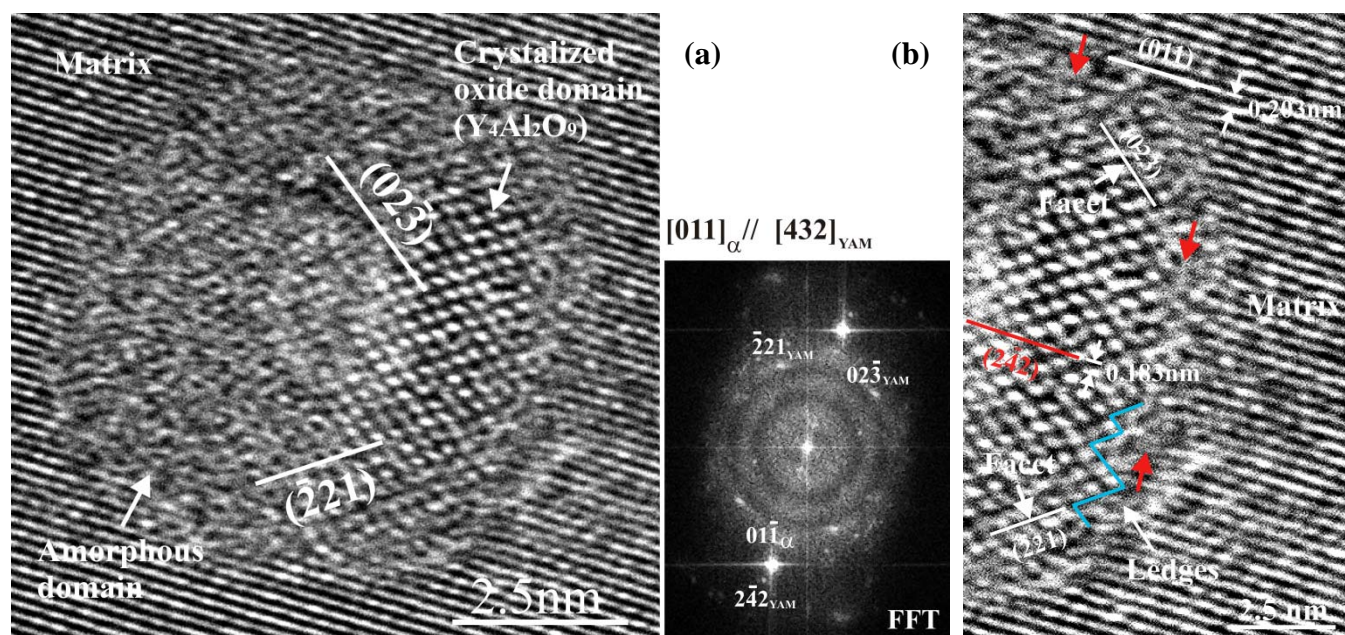


Fig. 3. HRTEM image shows a crystalline $Y_4Al_2O_9$ domain (2 x 5 nm) formed in an amorphous oxide particle and (b) an interfacial structure between the crystalline domain and the matrix. Facets, ledges, dislocations, and thin shell of amorphous domains (marked by red arrows) can be found at the interfaces. Orientation relationship between the $Y_4Al_2O_9$ crystalline domain and the matrix can be derived from the FFT image.

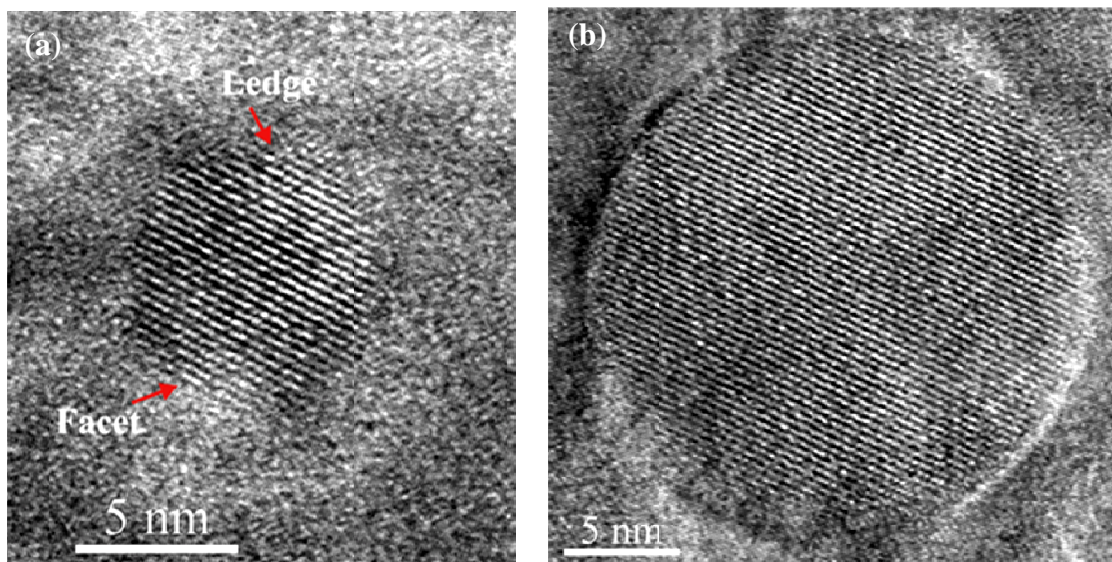


Fig. 4. HRTEM images of (a) a small nanoparticle ($d < 10$ nm) and (b) a large nanoparticle ($d > 20$ nm) and after prolonged annealing at 900 °C for 168 hours. Notice that the small nanoparticle remains faceted and the large nanoparticle becomes perfectly spherical and fully crystallized without a core/shell structure.

ACKNOWLEDGEMENTS

This work was performed under the auspices of the U.S. Department of Energy by Lawrence Livermore National Laboratory under Contract DE-AC52-07NA27344. Work at LLNL was funded by the Laboratory Directed Research and Development Program at LLNL under project tracking code 09-SI-003. The authors gratefully acknowledge Mark A. Wall for his TEM analysis of nanoparticle size distributions, and Nick E. Teslich and Rick J. Gross for TEM sample preparations.

REFERENCES

1. K. Ehrlich, *Phil. Trans. R. Soc. Lond. A* 357 (1999) 595.
2. S. Ukai, M. Fujiwara, *J. Nucl. Mater.* 307-311 (2002) 749.
3. R. Kasada, N. Toda, K. Yutani, H.S. Cho, H. Kishimoto, A. Kimura, *J. Nucl. Mater.* 341 (2005) 103.
4. T. Okuda, M. Fujiwara, *J. Mater. Sci. Lett.* 14 (1995) 1600.
5. Y. Kimura, S. Takaki, S. Suejima, R. Uemori, H. Tamehiro, *ISIJ International*, 39 (2) (1999) 176.
6. H. Sakasegawa, M. Tamura, S. Ohtsuka, S. Ukai, H. Tanigawa, A. Kohyama, M. Fujiwara, *J. Alloys & Compounds* 452 (2008) 2.
7. E. A. Marquis, *Appl. Phys. Lett.* 93 (2008) 181904.
8. M. Klimiankou, R. Lindau, A. Möslang, *J. Nucl. Mater.* 386-388 (2009) 553.
9. S. Uki, T. Nishida, H. Okada, T. Okuda, M. Fujiwara, K. Asabe, *J. Nucl. Sci. Technol.* 34 (3) (1997) 256.
10. K. Yutani, H. Kishimoto, R. Kasada, A. Kimura, *J. Nucl. Mater.* 367-370 (2007) 423.
11. A. Nørlund Christensen and R.G. Hazell, *Acta Chemica Scandinavica* 45 (1991) 226.
12. W.Y. Ching, Y.N. Xu, *Physical Review B* 59 (20) (1999) 12815.
13. V. de Castro, T. Leguey, M.A. Monge, A. Munoz, R. Pareja, D.R. Amador, J.M. Torralba, M. Victoria, *J. Nucl. Mater.* 322 (2003) 228.
14. C. Suryanarayana, *Prog. in Mater. Sci.* 46 (2001) 1.